

Supplementary Materials for
A 6G meta-device for 3D varifocal

Jing Cheng Zhang *et al.*

Corresponding author: Din Ping Tsai, dptsai@cityu.edu.hk; Chi Hou Chan, eechic@cityu.edu.hk

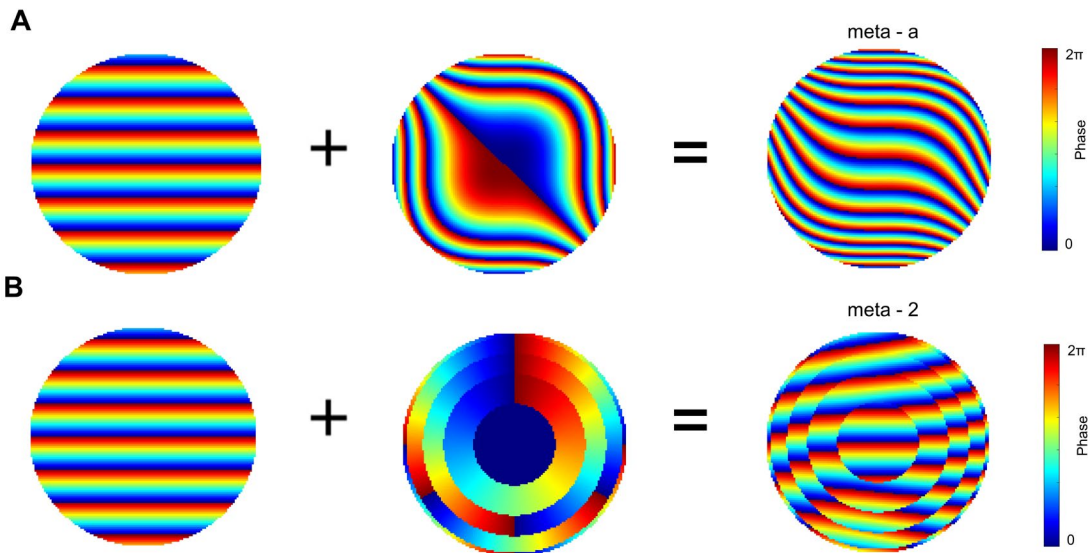
Sci. Adv. **9**, eadf8478 (2023)
DOI: 10.1126/sciadv.adf8478

This PDF file includes:

Notes S1 to S4
Figs. S1 to S9
Tables S1 to S4
References

Note S1. Synthetic-phase metasurfaces

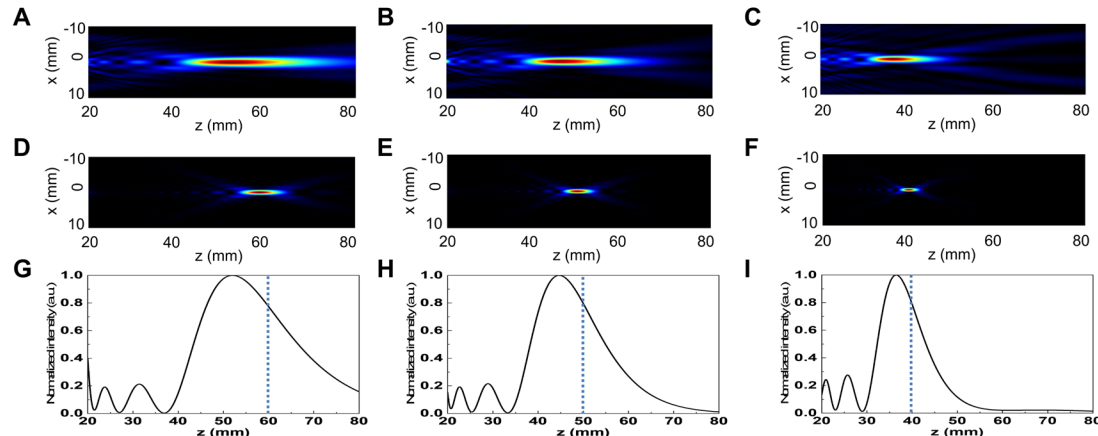
The combination of multiple metasurfaces brings versatile functions and applications. It is of great significance to reduce the number of metasurfaces while maintaining their rich functionalities. Here we demonstrated that by integrating two phase profiles into a single metasurface, these phase profiles could work well independently. The meta - a phase profile is the sum of a gradient phase profile for beam steering and a cubic phase profile for Airy beam generation (Fig. S1A). The phase profile of meta- 2 is obtained by adding the gradient phase profile for beam steering and a focusing phase profile for focal spot generation (Fig. S1B). We show that the experimental results of both the meta-device for varifocal Airy beam focal spot generation in a 2D plane and the meta-device for focal spot manipulation in 3D space match the theoretical ones (Fig. 4,5). The most immediate benefit is that the varifocal meta-device becomes much more compact and easier to integrate into devices like future 6G communication systems and advanced imaging systems.



Supplementary Figure S1 | Illustration of the combination of phase profiles for synthetic functions in a single metasurface. (A) The phase profile of meta - a (right) is synthesized by a gradient phase (left) and a cubic phase (middle). **(B)** the phase profile of meta - 2 (right) is synthesized by a gradient phase (left) and a spherical focusing lens (middle).

Note S2. Discussion on the focal length and accessible area of the varifocal meta-devices

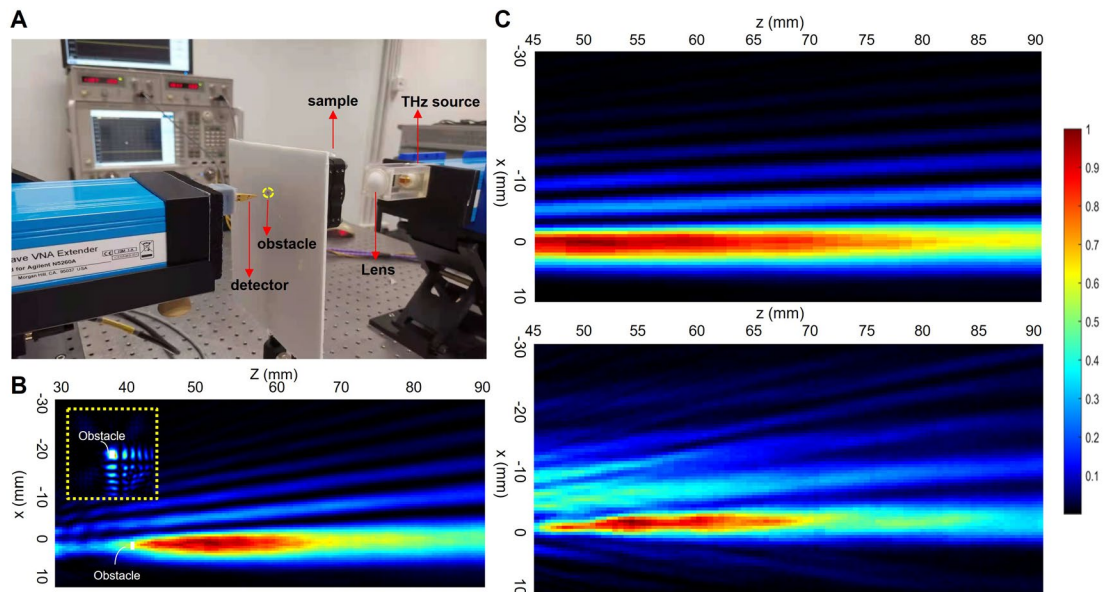
For the meta-device for focal spot manipulation in 3D space, the designed range of the focal length is from 40 mm to 60 mm. We first perform the theoretical calculations and show theoretical intensity distributions in x-z plane when the focal length is set to 60 mm, 50 mm, and 40 mm, shown in Fig. S2A, 2B and 2C (or upper panel of the Fig.5D, 5E and 5F), respectively. We notice that there is a slight mismatch between the focal length we set and that in the theoretically calculated results. Such a disagreement is reasonable, as the authors previously discussed in Figure S14 of (60), since when the meta-lens is small, the intensity peak will be less than the designed focal length. For more proof, we double the meta-device, and the corresponding theoretically calculated results are shown in Fig. S2D, S2E, and S2F, when the focal lengths are 60 mm, 50 mm, and 40 mm, respectively. This confirms that our Fresnel diffraction algorithm is correct. And we choose the minimum (40 mm), the maximum (60 mm), and a value in between (50 mm) to do measurements to verify the design. Fig. S2G, 2H, 2I show the measured intensity distributions when $x = y = 0$ (extracted from data shown in Fig. 5D, 5E and 5F, respectively). The dashed lines here indicate 80% of the maximum intensity, which we adopt as the maximum access area.



Supplementary Figure S2 | Discussion on the focal length and accessible area of the varifocal meta-devices. (A-C) Theoretical intensity distributions in the x-z plane when the focal length is set to 60 mm (A), 50 mm (B), and 40 mm (C), respectively. (D-F) Theoretical intensity distributions of the double-diameter meta-device in the x-z plane when the focal length is 60 mm (D), 50 mm (E), and 40 mm (F), respectively. g-i) The measured intensity distributions ($x = y = 0$), corresponding to the (A), (B), and (C), respectively.

Note S3. Self-healing property of the generated Airy beam

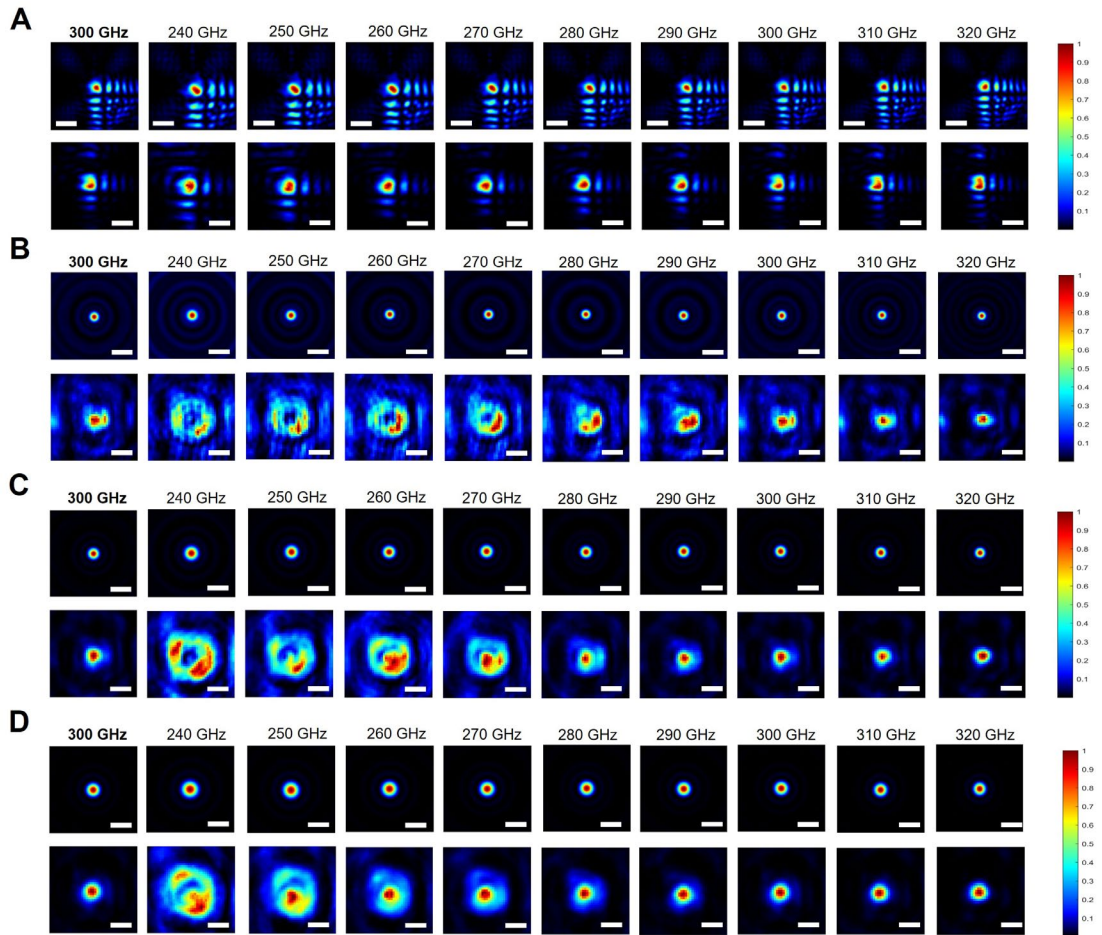
The self-healing property of the Airy beam is essential for the stable transmission of THz signals. Here, we perform experiments to verify the Airy beam's self-healing property, when the focal spot is in the zero-order diffraction. Fig. S3A shows the experiment setup. We place a piece of foam board between the sample and the detector. And we put a stripe of copper foil onto the foam board. The copper foil works as an obstacle to block the THz wave. The foam board could work as a support frame because it is transparent to the working wavelengths. The obstacle is set to block the main lobe of the generated Airy beam. The size of the obstacle is $3\lambda \times 3\lambda$, and Fig. S3B shows its position. Fig. S3C shows the measured intensity distributions in the x - z plane without and with the obstacle. From the bottom part of Fig. S3C, we could find that the measured intensity decreases sharply and then quickly recover when the obstacle blocks the main lobe of the Airy beam. Thus, the self-healing property of the generated Airy beam is validated.



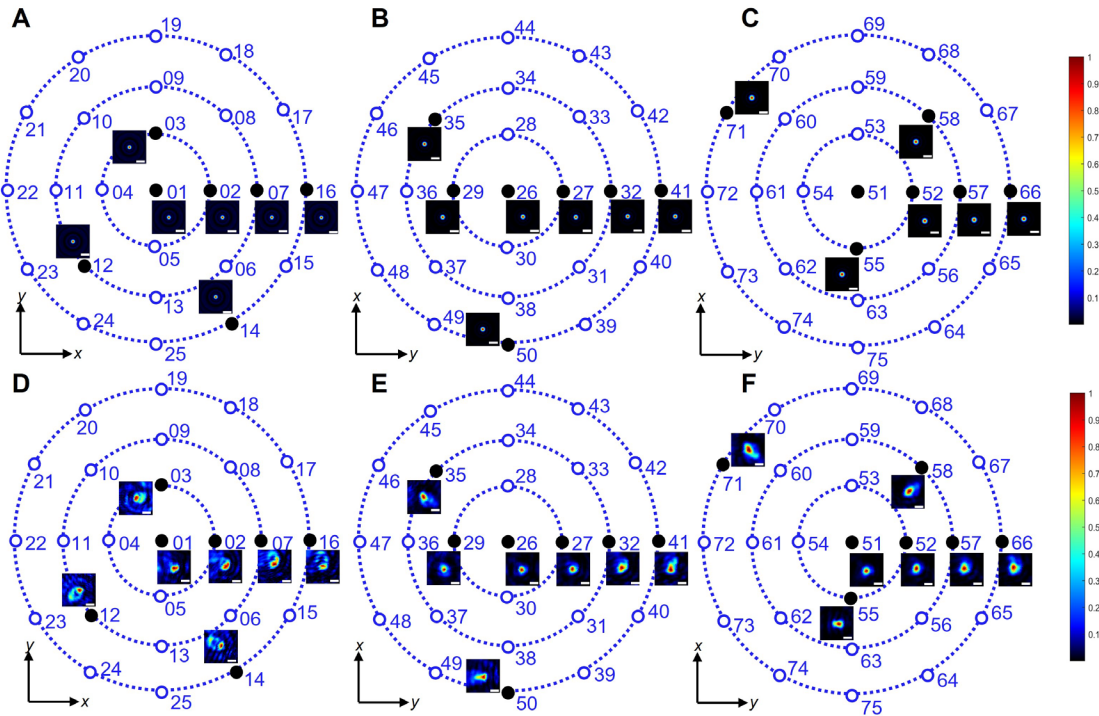
Supplementary Figure S3 | Validation of the self-healing property of the Airy beam.
(A) The experimental setup. **(B)** Illustration of the placement of the obstacle. The size of the obstacle is $3\text{ mm} \times 3\text{ mm}$ ($3\lambda \times 3\lambda$). **(C)** Measured intensity distributions in the x - z plane without the obstacle (**top**) and with the obstacle (**bottom**).

Note S4. Broadband property of the varifocal meta-device

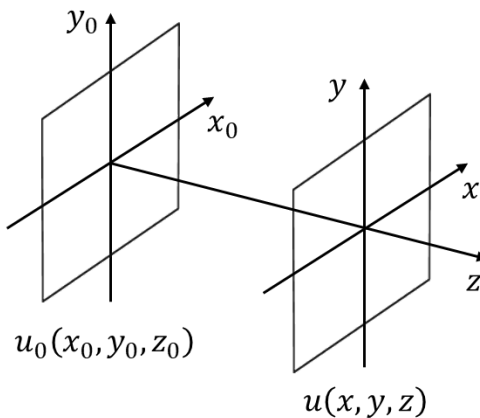
Broadband characteristics can effectively broaden the operating range of the device. The most apparent benefit of the broadband performance of the metasurfaces is wavelength multiplexing. Wavelength multiplexing can significantly increase the transmission capacity in a THz communication system. Here, we conducted experiments to check the performance of the broadband characteristics of our varifocal meta-device. From Fig. S4, we find that the Airy beam varifocal meta-device works well throughout the whole measured band (Fig. S4A); while the other could work from 290 - 320 THz, 280 – 320 THz, and 250-320 THz when the focal length is 40 mm (Fig. S4B), 50 mm (Fig. S4C), and 60 mm (Fig. S4D) respectively.



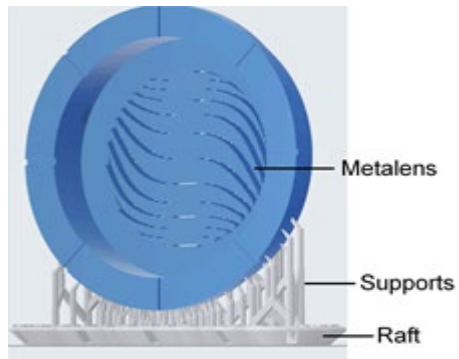
Supplementary Figure S4 | Broadband property of the varifocal meta-device. **(A)** Airy beam varifocal meta-device, from 240 GHz to 320 GHz. **(B)** The meta-device for focal spot manipulation in 3D space, from 240 GHz to 320 GHz, when the focal length is 40 mm. **(C)** The meta-device for focal spot manipulation in 3D space, from 240 GHz to 320 GHz, when the focal length is 50 mm. **(D)** The meta-device for focal spot manipulation in 3D space, from 240 GHz to 320 GHz, when the focal length is 60 mm. The top is the theoretical results for these four parts, and the bottom is the measured results. The scalar bar is 5 mm.



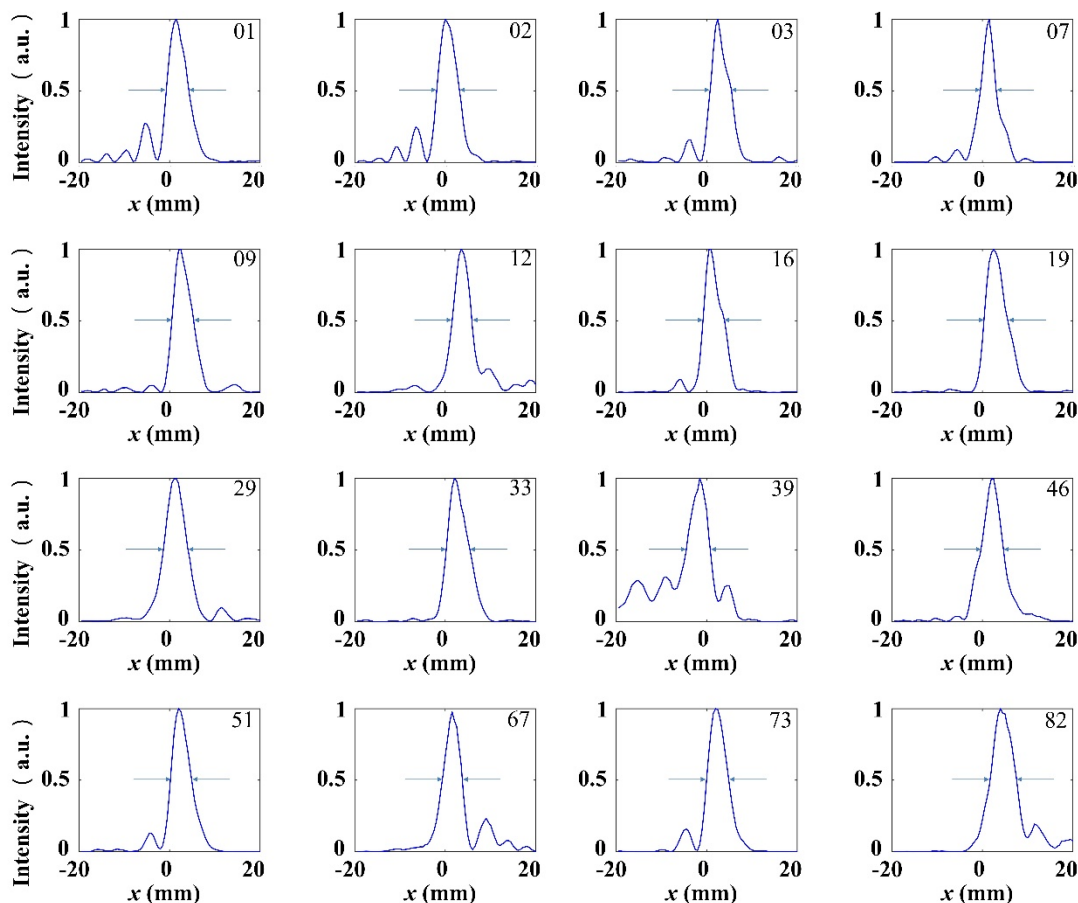
Supplementary Figure S5 | Performances of the 3D varifocal meta-device. (A-C) Theoretical results for arbitrary focal spots in 3D space. (A) $f = 40$ mm. (B) $f = 50$ mm. (C) $f = 60$ mm. (D-F) Experimental results for arbitrary focal spots in 3D space. (D) $f = 40$ mm. (E) $f = 50$ mm. (F) $f = 60$ mm. The scalar bar is 5 mm.



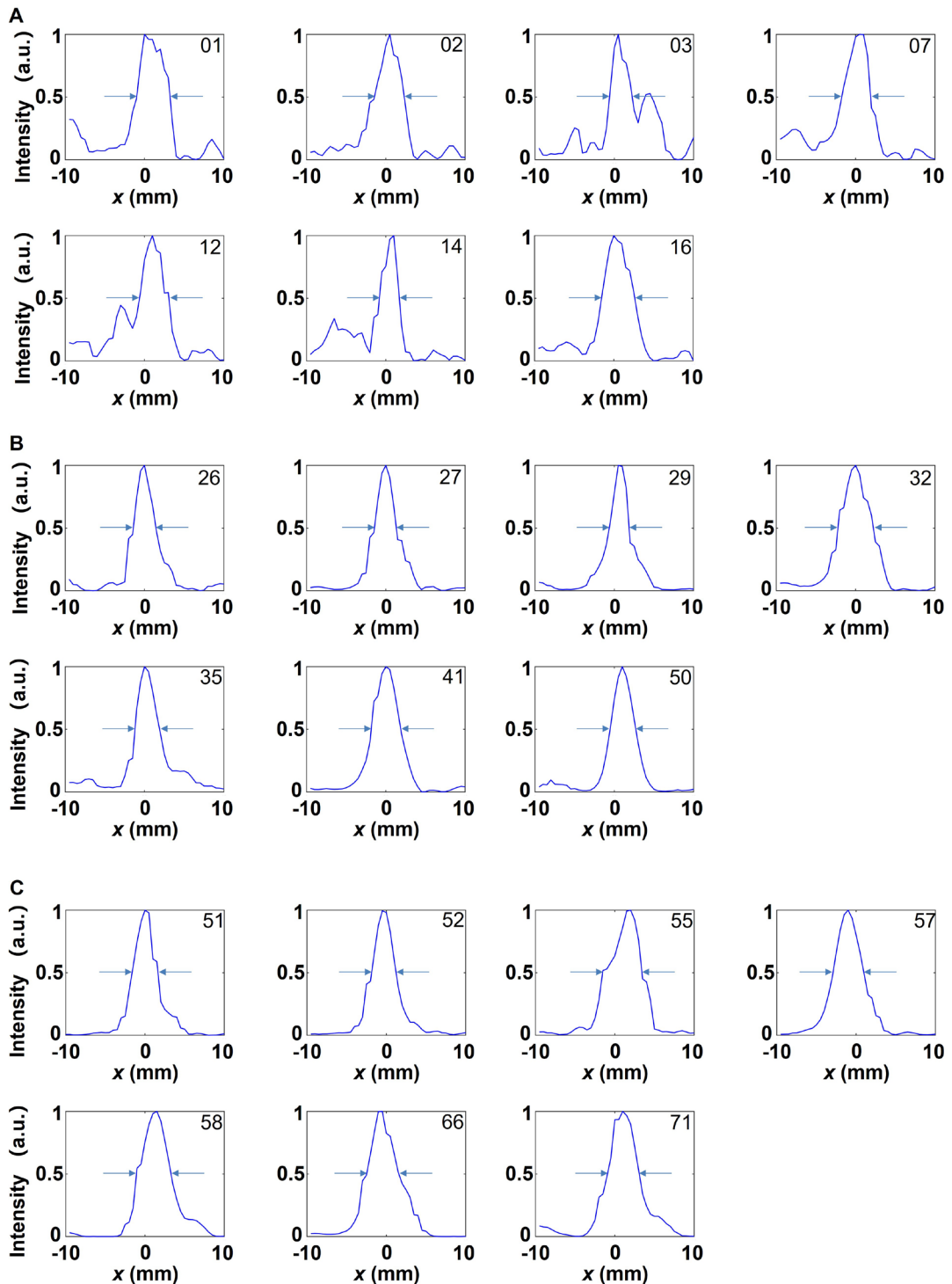
Supplementary Figure S6 | Sketch of the THz wave transmission. Here, $u_0(x_0, y_0, z_0)$ defines the incident plane and $u(x, y, z)$ determines the plane of emergence.



Supplementary Figure S7 | The 3D model of the metasurface in the 3D printing process.



Supplementary Figure S8 | Field profiles of the main lobes of the Airy beam. The figure shows the lines parallel to the x-axis and passing through the intensity maximum in Fig. 4C. The label in the upper right corner of each figure is consistent with that in Fig. 4C. The arrows indicate the full width at half maximum (FWHM). The values of the FWHM can be found in Supplementary Table S3. The coordinates in the figure are relative coordinate systems, and their actual coordinates are consistent with that in Fig. 4C.



Supplementary Figure S9 | Field profiles of the focal spots in 3D space. (A-C) shows the lines parallel to the x-axis and passing through the intensity maximum in Fig. 5A to 5C, respectively. The label in the upper right corner of each figure is consistent with that in Fig. 5A to 5C. The arrows indicate the full width at half maximum (FWHM). The values of the FWHM can be found in Supplementary Table S4. The coordinates in the figure are relative coordinate systems, and their actual coordinates are consistent with that in Fig. 5A to 5C.

Supplementary Table S1 | Handbook for Airy beam focal spot manipulation.

No.	(x, y) / mm	(θ_1, θ_2) / rad	No.	(x, y) / mm	(θ_1, θ_2) / rad	No.	(x, y) / mm	(θ_1, θ_2) / rad
1	(0, 0)	(1.57, -1.57)	30	(2.03, 0.84)	(1.178, -0.393)	58	(-2.18, -1.58)	(-1.923, -3.104)
2	(0.7, 0)	(1.376, -1.376)	31	(1.56, 1.56)	(1.57, 0)	59	(-1.59, -2.18)	(-1.609, -2.790)
3	(0, 0.7)	(2.947, 0.195)	32	(0.84, 2.03)	(1.964, 0.393)	60	(-0.83, -2.57)	(-1.294, -2.476)
4	(-0.7, 0)	(-1.766, 1.766)	33	(0, 2.2)	(2.356, 0.785)	61	(0, -2.7)	(-0.980, -2.161)
5	(0, -0.7)	(-0.195, -2.947)	34	(-0.84, 2.03)	(2.749, 1.178)	62	(0, 0)	(-0.911, -1.697)
6	(0.85, -0.85)	(1.964, -0.393)	35	(-1.56, 1.56)	(3.14, 1.57)	63	(0, 0)	(-0.660, -1.445)
7	(1.2, 0)	(1.178, -1.178)	36	(-2.03, 0.84)	(-2.749, 1.964)	64	(0, 0)	(-0.408, -1.178)
8	(0.85, 0.85)	(0.393, -1.964)	37	(-2.2, 0)	(-2.356, 2.356)	65	(0, 0)	(-0.126, -0.911)
9	(0, 1.2)	(-0.393, -2.749)	38	(-2.03, -0.84)	(-1.964, 2.749)	66	(0, 0)	(0.126, -0.660)
10	(-0.85, 0.85)	(-1.178, 2.749)	39	(-1.56, -1.56)	(-1.57, 3.14)	67	(3, 0)	(0.393, -0.393)
11	(-1.2, 0)	(-1.964, 1.964)	40	(-0.84, -2.03)	(-1.178, -2.670)	68	(2.9, 0.78)	(0.660, -0.126)
12	(-0.85, -0.85)	(-2.749, 1.178)	41	(0, -2.2)	(-0.785, -2.356)	69	(2.6, 1.5)	(0.911, 0.126)
13	(0, -1.2)	(2.749, 0.393)	42	(0.83, -2.57)	(-0.666, -1.847)	70	(2.12, 2.12)	(1.178, 0.393)
14	(0.85, -1.47)	(-0.063, -2.011)	43	(1.59, -2.18)	(-0.352, -1.533)	71	(1.5, 2.6)	(1.439, 0.660)
15	(1.47, -0.85)	(0.440, 1.508)	44	(2.18, -1.59)	(-0.038, -1.219)	72	(0.78, 2.9)	(1.697, 0.911)
16	(1.7, 0)	(0.974, -0.974)	45	(2.56, -0.83)	(0.277, -0.905)	73	(0, 3)	(1.979, 1.178)
17	(1.47, 0.85)	(1.477, -0.440)	46	(2.7, 0)	(0.591, -0.591)	74	(-0.78, 2.9)	(2.231, 1.445)
18	(0.85, 1.47)	(2.011, 0.063)	47	(2.57, 0.83)	(0.905, -0.277)	75	(-1.5, 2.6)	(2.482, 1.697)
19	(0, 1.7)	(2.545, 0.597)	48	(2.18, 1.59)	(1.219, 0.038)	76	(-2.12, 2.12)	(2.765, 1.964)
20	(-0.85, 1.47)	(3.047, 1.131)	49	(1.59, 2.18)	(1.533, 0.352)	77	(-2.6, 1.5)	(3.016, 2.231)
21	(-1.47, 0.85)	(-2.670, 1.634)	50	(0.83, 2.57)	(1.847, 0.666)	78	(-2.9, 0.78)	(-3.016, 2.482)
22	(-1.7, 0)	(-2.168, 2.168)	51	(0, 2.7)	(2.161, 0.980)	79	(-3, 0)	(-2.765, 2.749)
23	(-1.47, -0.85)	(-1.634, 2.670)	52	(-0.83, 2.57)	(2.476, 1.294)	80	(-2.9, -0.78)	(-2.482, 3.016)
24	(-0.85, -1.47)	(-1.131, -3.079)	53	(-1.59, 2.18)	(2.790, 1.609)	81	(-2.6, -1.5)	(-2.231, -3.016)
25	(0, -1.7)	(-0.597, -2.545)	54	(-2.18, 1.59)	(3.104, 1.923)	82	(-2.12, -2.12)	(-1.979, -2.749)
26	(0.84, -2.03)	(-0.393, -1.964)	55	(-2.56, 0.83)	(-2.865, 2.237)	83	(-1.5, -2.6)	(-1.697, -2.482)
27	(1.56, -1.56)	(0, -1.57)	56	(-2.7, 0)	(-2.551, 2.551)	84	(-0.78, -2.9)	(-1.445, -2.231)
28	(2.03, -0.84)	(0.393, -1.178)	57	(-2.57, -0.83)	(-2.237, 2.865)	85	(0, -3)	(-1.194, -1.964)
29	(2.2, 0)	(0.785, -0.785)						

Supplementary Table S2 | Handbook for focal spot manipulation in 3D space.

No.	(x, y) / mm	(θ_1 , θ_2) / rad	No.	(x, y) / mm	(θ_1 , θ_2) / rad	No.	(x, y) / mm	(θ_1 , θ_2) / rad
1	(0, 0)	(1.57, -1.57)	26	(0, 0)	(1.57, -1.57)	51	(0, 0)	(1.57, -1.57)
2	(9.5, 0)	(1.052, -1.052)	27	(12, 0)	(2.105, -2.105)	52	(14, 0)	(2.105, -2.105)
3	(0, 9.5)	(2.623, 0.518)	28	(0, 12)	(-2.608, -0.534)	53	(0, 14)	(-2.608, -0.534)
4	(9.5, 0)	(-2.089, 2.089)	29	(-12, 0)	(-1.037, 1.037)	54	(-14, 0)	(-1.037, 1.037)
5	(0, -9.5)	(-0.518, -2.623)	30	(0, -12)	(0.534, 2.608)	55	(0, -14)	(0.534, 2.608)
6	(10.96, -10.96)	(-0.267, -1.304)	31	(15.2, -15.2)	(0.251, -1.822)	56	(18.03, -18.03)	(0.251, -1.822)
7	(15.5, 0)	(0.518, -0.518)	32	(21.5, 0)	(1.037, -1.037)	57	(25.5, 0)	(1.037, -1.037)
8	(10.96, 10.96)	(1.304, 0.267)	33	(15.2, 15.2)	(1.822, -0.251)	58	(18.03, 18.03)	(1.822, -0.251)
9	(0, 15.5)	(2.089, 1.052)	34	(0, 21.5)	(2.608, 0.534)	59	(0, 25.5)	(2.608, 0.534)
10	(-10.96, 10.96)	(2.875, 1.838)	35	(-15.2, 15.2)	(-2.89, 1.320)	60	(-18.03, -18.03)	(-2.89, 1.32)
11	(-15.5, 0)	-2.623, 2.623)	36	(-21.5, 0)	(-2.105, 2.105)	61	(-25.5, 0)	(-2.105, 2.105)
12	(-10.96, -10.96)	(-1.838, -2.875)	37	(-15.2, -15.2)	(-1.32, 2.89)	62	(-18.31, -18.31)	(-1.32, 2.89)
13	(0, -15.5)	(-1.052, -2.089)	38	(0, -21.5)	(-0.534, -2.608)	63	(0, -25.5)	(-0.534, -2.608)
14	(10, -17.32)	(-1.047, -1.047)	39	(12.5, -21.65)	(-1.047, -1.047)	64	(15.5, -26.847)	(-1.047, -1.047)
15	(17.32, -10)	(-0.524, -0.524)	40	(21.65, -12.5)	(-0.524, -0.524)	65	(26.847, -15.5)	(-0.524, -0.524)
16	(20, 0)	(0, 0)	41	(25, 0)	(0, 0)	66	(31, 0)	(0, 0)
17	(17.32, 10)	(0.52, 0.52)	42	(21.65, 12.5)	(0.524, 0.524)	67	(26.847, 15.5)	(0.524, 0.524)
18	(10, 17.32)	(1.047, 1.047)	43	(12.5, 21.65)	(1.047, 1.047)	68	(15.5, 26.847)	(1.047, 1.047)
19	(0, 20)	(1.57, 1.57)	44	(0, 25)	(1.571, 1.571)	69	(0, 31)	(1.571, 1.571)
20	(-10, 17.32)	(2.094, 2.094)	45	(-12.5, 21.65)	(2.094, 2.094)	70	(-15.5, 26.847)	(2.094, 2.094)
21	(-17.32, 10)	(2.618, 2.618)	46	(-21.65, 12.5)	(2.618, 2.618)	71	(-26.847, 15.5)	(2.618, 2.618)
22	(-20, 0)	(3.141, 3.141)	47	(-25, 0)	(3.142, 3.142)	72	(-31, 0)	(3.142, 3.142)
23	(-17.32, -10)	(-2.618, -2.618)	48	(-21.65, -12.5)	(-2.618, -2.618)	73	(-26.847, -15.5)	(-2.618, -2.618)
24	(-10, -17.32)	(-2.094, -2.094)	49	(-12.5, -21.65)	(-2.094, -2.094)	74	(-15.5, -26.847)	(-2.094, -2.094)
25	(0, -20)	(-1.571, -1.571)	50	(0, -25)	(-1.571, -1.571)	75	(0, -31)	(-1.571, -1.571)

Supplementary Table S3 | FWHM of field profiles of the main lobes of the generated Airy beam.

No.	FWHM (mm)						
1	4.5	2	5	3	4.5	7	3.5
9	5	12	4.5	16	4.5	19	5
29	6	33	4.5	39	5	46	4.5
51	4.5	67	4	73	5	82	5

Supplementary Table S4 | FWHM of field profiles of the focal spots in 3D space.

No.	FWHM (mm)						
1	4.5	2	4	3	3	7	3.5
12	3.5	14	2	16	4	26	3.5
27	3	29	2.5	32	4.5	35	3
41	3	50	5	51	3	52	3
55	4.5	57	3.5	58	3.5	66	4
71	4						

REFERENCES

1. S. Dang, O. Amin, B. Shihada, M.-S. Alouini, What should 6g be? *Nat. Electron.* **3**, 20–29 (2020).
2. X. You, C.-X. Wang, J. Huang, X. Gao, Z. Zhang, M. Wang, Y. Huang, C. Zhang, Y. Jiang, J. Wang, M. Zhu, B. Sheng, D. Wang, Z. Pan, P. Zhu, Y. Yang, Z. Liu, P. Zhang, X. Tao, S. Li, Z. Chen, X. Ma, C.-L. I, S. Han, K. Li, C. Pan, Z. Zheng, L. Hanzo, X. Shen, Y. J. Guo, Z. Ding, H. Haas, W. Tong, P. Zhu, G. Yang, J. Wang, E. G. Larsson, H. Q. Ngo, W. Hong, H. Wang, D. Hou, J. Chen, Z. Chen, Z. Hao, G. Y. Li, R. Tafazolli, Y. Gao, H. V. Poor, G. P. Fettweis, Y.-C. Liang, Towards 6g wireless communication networks: Vision, enabling technologies, and new paradigm shifts. *Sci. China Inf. Sci.* **64**, 110301 (2020).
3. L. Cong, R. Singh, Spatiotemporal dielectric metasurfaces for unidirectional propagation and reconfigurable steering of terahertz beams. *Adv. Mater.* **32**, e2001418 (2020).
4. X. Y. Peng, R. Jung, T. Toncian, O. Willi, J. H. Teng, Distortion of the intense terahertz signal measured by spectral-encoding technique. *Appl. Phys. Lett.* **94**, 221107 (2009).
5. H. J. Song, N. Lee, Terahertz communications: Challenges in the next decade. *IEEE Trans Terahertz Sci Technol.* **12**, 105–117 (2022).
6. P. del Hougne, G. Lerosey, Leveraging chaos for wave-based analog computation: Demonstration with indoor wireless communication signals. *Phys. Rev. X* **8**, 041037 (2018).
7. V. C. Su, C. H. Chu, G. Sun, D. P. Tsai, Advances in optical metasurfaces: Fabrication and applications [invited]. *Opt. Express* **26**, 13148–13182 (2018).
8. H. H. Hsiao, C. H. Chu, D. P. Tsai, Fundamentals and applications of metasurfaces. *Small Methods* **1**, 1600064 (2017).
9. M. K. Chen, Y. F. Wu, L. Feng, Q. B. Fan, M. H. Lu, T. Xu, D. P. Tsai, Principles, functions, and applications of optical meta-lens. *Adv. Opt. Mater.* **9**, 2001414 (2021).

10. M. R. Akram, G. Ding, K. Chen, Y. Feng, W. Zhu, Ultrathin single layer metasurfaces with ultra-wideband operation for both transmission and reflection. *Adv. Mater.* **32**, e1907308 (2020).
11. Q. Cheng, M. Ma, D. Yu, Z. Shen, J. Xie, J. Wang, N. Xu, H. Guo, W. Hu, S. Wang, T. Li, S. Zhuang, Broadband achromatic metalens in terahertz regime. *Sci. Bull.* **64**, 1525–1531 (2019).
12. D. Wang, Y. Hwang, Y. Dai, G. Si, S. Wei, D. Y. Choi, D. E. Gomez, A. Mitchell, J. Lin, X. Yuan, Broadband high-efficiency chiral splitters and holograms from dielectric nanoarc metasurfaces. *Small* **15**, e1900483 (2019).
13. K. Huang, F. Qin, H. Liu, H. Ye, C. W. Qiu, M. Hong, B. Luk'yanchuk, J. Teng, Planar diffractive lenses: Fundamentals, functionalities, and applications. *Adv. Mater.* **30**, e1704556 (2018).
14. L. Ding, X. S. Luo, L. Cheng, M. Thway, J. F. Song, S. J. Chua, E. E. M. Chia, J. H. Teng, Electrically and thermally tunable smooth silicon metasurfaces for broadband terahertz antireflection. *Adv. Opt. Mater.* **6**, 1800928 (2018).
15. G. B. Wu, Y. S. Zeng, K. F. Chan, S. W. Qu, C. H. Chan, 3-D printed circularly polarized modified fresnel lens operating at terahertz frequencies. *IEEE Trans. Antennas Propag.* **67**, 4429–4437 (2019).
16. S. Jahani, S. Kim, J. Atkinson, J. C. Wirth, F. Kalhor, A. A. Noman, W. D. Newman, P. Shekhar, K. Han, V. Van, R. G. DeCorby, L. Chrostowski, M. Qi, Z. Jacob, Controlling evanescent waves using silicon photonic all-dielectric metamaterials for dense integration. *Nat. Commun.* **9**, 1893 (2018).
17. W. D. Newman, C. L. Cortes, A. Afshar, K. Cadien, A. Meldrum, R. Fedosejevs, Z. Jacob, Observation of long-range dipole-dipole interactions in hyperbolic metamaterials. *Sci. Adv.* **4**, eaar5278 (2018).

18. M. S. Hwang, H. C. Lee, K. H. Kim, K. Y. Jeong, S. H. Kwon, K. Koshelev, Y. Kivshar, H. G. Park, Ultralow-threshold laser using super-bound states in the continuum. *Nat. Commun.* **12**, 4135 (2021).
19. Y. Jahani, E. R. Arvelo, F. Yesilkoy, K. Koshelev, C. Cianciaruso, M. De Palma, Y. Kivshar, H. Altug, Imaging-based spectrometer-less optofluidic biosensors based on dielectric metasurfaces for detecting extracellular vesicles. *Nat. Commun.* **12**, 3246 (2021).
20. S. Han, L. Cong, Y. K. Srivastava, B. Qiang, M. V. Rybin, A. Kumar, R. Jain, W. X. Lim, V. G. Achanta, S. S. Prabhu, Q. J. Wang, Y. S. Kivshar, R. Singh, All-dielectric active terahertz photonics driven by bound states in the continuum. *Adv. Mater.* **31**, e1901921 (2019).
21. E. Galiffi, P. A. Huidobro, J. B. Pendry, An archimedes' screw for light. *Nat. Commun.* **13**, 2523 (2022).
22. S. Jahani, Z. Jacob, All-dielectric metamaterials. *Nat. Nanotechnol.* **11**, 23–36 (2016).
23. B. H. Cheng, H. W. Chen, K. J. Chang, Y. C. Lan, D. P. Tsai, Magnetically controlled planar hyperbolic metamaterials for subwavelength resolution. *Sci. Rep.* **5**, 18172 (2015).
24. I. Ghimire, J. Y. Yang, S. Gurung, S. K. Mishra, H. W. H. Lee, Polarization-dependent photonic crystal fiber optical filters enabled by asymmetric metasurfaces. *Nanophotonics* **11**, 2711–2717 (2022).
25. B. H. Chen, P. C. Wu, V. C. Su, Y. C. Lai, C. H. Chu, I. C. Lee, J. W. Chen, Y. H. Chen, Y. C. Lan, C. H. Kuan, D. P. Tsai, Gan metalens for pixel-level full-color routing at visible light. *Nano Lett.* **17**, 6345–6352 (2017).
26. H.-H. Wu, B. H. Cheng, Y.-C. Lan, Coherent-controlled all-optical devices based on plasmonic resonant tunneling waveguides. *Plasmonics* **12**, 2005–2011 (2017).
27. T. J. Yen, W. J. Padilla, N. Fang, D. C. Vier, D. R. Smith, J. B. Pendry, D. N. Basov, X. Zhang, Terahertz magnetic response from artificial materials. *Science* **303**, 1494–1496 (2004).

28. S. Wang, P. C. Wu, V. C. Su, Y. C. Lai, M. K. Chen, H. Y. Kuo, B. H. Chen, Y. H. Chen, T. T. Huang, J. H. Wang, R. M. Lin, C. H. Kuan, T. Li, Z. Wang, S. Zhu, D. P. Tsai, A broadband achromatic metalens in the visible. *Nat. Nanotechnol.* **13**, 227–232 (2018).
29. R. J. Lin, V. C. Su, S. Wang, M. K. Chen, T. L. Chung, Y. H. Chen, H. Y. Kuo, J. W. Chen, J. Chen, Y. T. Huang, J. H. Wang, C. H. Chu, P. C. Wu, T. Li, Z. Wang, S. Zhu, D. P. Tsai, Achromatic metalens array for full-colour light-field imaging. *Nat. Nanotechnol.* **14**, 227–231 (2019).
30. L. Li, Z. Liu, X. Ren, S. Wang, V. C. Su, M. K. Chen, C. H. Chu, H. Y. Kuo, B. Liu, W. Zang, G. Guo, L. Zhang, Z. Wang, S. Zhu, D. P. Tsai, Metalens-array-based high-dimensional and multiphoton quantum source. *Science* **368**, 1487–1490 (2020).
31. J. Tao, Q. You, Z. Li, M. Luo, Z. Liu, Y. Qiu, Y. Yang, Y. Zeng, Z. He, X. Xiao, G. Zheng, S. Yu, Mass-manufactured beam-steering metasurfaces for high-speed full-duplex optical wireless-broadcasting communications. *Adv. Mater.* **34**, e2106080 (2022).
32. S. Venkatesh, X. Y. Lu, H. Saeidi, K. Sengupta, A high-speed programmable and scalable terahertz holographic metasurface based on tiled cmos chips. *Nat. Electron.* **3**, 785–793 (2020).
33. N. Hasegawa, Y. Ohta, 2-Dimensional simple beam steering for large-scale antenna on microwave power transfer. *IEEE Trans. Microwave Theory Tech.* **70**, 2432–2441 (2022).
34. J. Yang, S. Gurung, S. Bej, P. Ni, H. W. Howard Lee, Active optical metasurfaces: Comprehensive review on physics, mechanisms, and prospective applications. *Rep. Prog. Phys.* **85**, 036101 (2022).
35. M. Bosch, M. R. Shcherbakov, K. Won, H. S. Lee, Y. Kim, G. Shvets, Electrically actuated varifocal lens based on liquid-crystal-embedded dielectric metasurfaces. *Nano Lett.* **21**, 3849–3856 (2021).

36. I. Kim, W. S. Kim, K. Kim, M. A. Ansari, M. Q. Mehmood, T. Badloe, Y. Kim, J. Gwak, H. Lee, Y. K. Kim, J. Rho, Holographic metasurface gas sensors for instantaneous visual alarms. *Sci. Adv.* **7**, eabe9943 (2021).
37. M. Y. Shalaginov, S. An, Y. Zhang, F. Yang, P. Su, V. Liberman, J. B. Chou, C. M. Roberts, M. Kang, C. Rios, Q. Du, C. Fowler, A. Agarwal, K. A. Richardson, C. Rivero-Baleine, H. Zhang, J. Hu, T. Gu, Reconfigurable all-dielectric metalens with diffraction-limited performance. *Nat. Commun.* **12**, 1225 (2021).
38. Q. Wang, E. T. F. Rogers, B. Gholipour, C.-M. Wang, G. Yuan, J. Teng, N. I. Zheludev, Optically reconfigurable metasurfaces and photonic devices based on phase change materials. *Nat. Photon.* **10**, 60–65 (2015).
39. S. M. Kamali, E. Arbabi, A. Arbabi, Y. Horie, A. Faraon, Highly tunable elastic dielectric metasurface lenses. *Laser Photonics Rev.* **10**, 1002–1008 (2016).
40. L. Li, J. Zhang, Y. Q. Hu, J. J. Lai, S. Wang, P. Yang, X. L. Li, H. G. Duan, Broadband polarization-switchable multi-focal noninterleaved metalenses in the visible. *Laser Photonics Rev.* **15**, 2100198 (2021).
41. S. Colburn, A. Zhan, A. Majumdar, Varifocal zoom imaging with large area focal length adjustable metalenses. *Optica* **5**, 825–831 (2018).
42. L. Zhang, X. Q. Chen, S. Liu, Q. Zhang, J. Zhao, J. Y. Dai, G. D. Bai, X. Wan, Q. Cheng, G. Castaldi, V. Galdi, T. J. Cui, Space-time-coding digital metasurfaces. *Nat. Commun.* **9**, 4334 (2018).
43. C. Huang, C. L. Zhang, J. N. Yang, B. Sun, B. Zhao, X. G. Luo, Reconfigurable metasurface for multifunctional control of electromagnetic waves. *Adv. Opt. Mater.* **5**, 1700485 (2017).
44. Q. Hu, J. M. Zhao, K. Chen, K. Qu, W. X. Yang, J. M. Zhao, T. Jiang, Y. J. Feng, An intelligent programmable omni-metasurface. *Laser Photonics Rev.* **16**, 2100718 (2022).

45. K. Chen, Y. Feng, F. Monticone, J. Zhao, B. Zhu, T. Jiang, L. Zhang, Y. Kim, X. Ding, S. Zhang, A. Alu, C. W. Qiu, A reconfigurable active huygens' metalens. *Adv. Mater.* **29**, 1606422 (2017).
46. A. Casolaro, A. Toscano, A. Alu, F. Bilotti, Dynamic beam steering with reconfigurable metagratings. *IEEE Trans. Antennas Propag.* **68**, 1542–1552 (2020).
47. A. Nemat, Q. Wang, M. H. Hong, J. H. Teng, Tunable and reconfigurable metasurfaces and metadevices. *Opto-Electron. Adv.* **1**, 18000901–18000925 (2018).
48. X. Fu, F. Yang, C. Liu, X. Wu, T. J. Cui, Terahertz beam steering technologies: From phased arrays to field-programmable metasurfaces. *Adv. Opt. Mater.* **8**, 1900628 (2019).
49. S. Liu, S. Ma, R. Shao, L. Zhang, T. Yan, Q. Ma, S. Zhang, T. J. Cui, Moiré metasurfaces for dynamic beamforming. *Sci. Adv.* **8**, eab01511 (2022).
50. H. Ai, Q. Kang, W. Wang, K. Guo, Z. Guo, Multi-beam steering for 6g communications based on graphene metasurfaces. *Sensors (Basel)* **21**, 4784 (2021).
51. Z. Chen, B. Ning, C. Han, Z. Tian, S. Li, Intelligent reflecting surface assisted terahertz communications toward 6g. *IEEE Wireless Commun.* **28**, 110–17 (2021).
52. X. Meng, M. Nekovee, D. Wu, The design and analysis of electronically reconfigurable liquid crystal-based reflectarray metasurface for 6g beamforming, beamsteering, and beamsplitting. *IEEE Access* **9**, 155564–155575 (2021).
53. Q. Q. Cheng, J. C. Wang, L. Ma, Z. X. Shen, J. Zhang, X. Y. Zheng, T. Chen, Y. Yu, D. Yu, Q. He, W. Hu, T. Li, S. L. Zhuang, L. Zhou, Achromatic terahertz airy beam generation with dielectric metasurfaces. *Nanophotonics* **10**, 1123–1131 (2021).
54. J. Iannacci, H. V. Poor, Review and perspectives of micro/nano technologies as key-enablers of 6g. *IEEE Access* **10**, 55428–55458 (2022).

55. J. Iannacci, The weaf mnecosystem: A perspective of mems/nems technologies as pillars of future 6g, tactile internet and super-iot. *Microsyst. Technol.* **27**, 4193–4207 (2021).
56. H. Y. Wang, J. Du, H. Wang, Y. H. Lu, P. Wang, Generation of spin-dependent accelerating beam with geometric metasurface. *Adv. Opt. Mater.* **7**, 1900552 (2019).
57. J. Wen, L. Chen, B. Yu, J. B. Nieder, S. Zhuang, D. Zhang, D. Lei, All-dielectric synthetic-phase metasurfaces generating practical airy beams. *ACS Nano* **15**, 1030–1038 (2021).
58. S. Bernet, W. Harm, M. Ritsch-Marte, Demonstration of focus-tunable diffractive Moiré-lenses. *Opt. Express* **21**, 6955–6966 (2013).
59. P. P. Banerjee, A simple derivation of the fresnel diffraction formula. *Proc. IEEE* **73**, 1859–1860 (1985).
60. M. Zhao, M. K. Chen, Z. P. Zhuang, Y. Zhang, A. Chen, Q. Chen, W. Liu, J. Wang, Z. M. Chen, B. Wang, X. Liu, H. Yin, S. Xiao, L. Shi, J. W. Dong, J. Zi, D. P. Tsai, Phase characterisation of metalenses. *Light: Sci. Appl.* **10**, 52 (2021).